Single-Layer, Unidirectional, Broadside-Radiating Planar Quadrupole Antenna for 5G IoT Applications

Rocio Rodriguez-Cano, *Student Member, IEEE*, Richard W. Ziolkowski, *Life Fellow, IEEE*

***Abstract*—In this paper, an innovative quadrupole-based broadside-radiating unidirectional antenna is designed at 28.475 GHz for 5G IoT applications. The planar antenna is based on a single-layer technology and realized on a flexible substrate to facilitate conformal applications. It consists of a coax-fed driven dipole and two quadrupolar near-field resonant parasitic (NFRP) elements. The broadside-radiating design achieves a unidirectional pattern with a realized gain of 4.85 dBi and a front-to-back ratio of 9.4 dB. The total efficiency of the antenna is 85%. A differential-fed prototype was designed, fabricated, and tested at 1.579 GHz to make the measurements more manageable. The measured and simulated results are in good agreement.**

***Index Terms*—Broadside radiation, high efficiency, Internet-of-Things (IoT), planar antennas, unidirectional pattern.**

I. Introduction

THE advent of the new fifth generation (5G) of mobile communications has opened a realm of possibilities to interconnect all of the electronic devices that surround us; thanks to the promised lower latency, higher capacity and increased bandwidth [1]–[3] in comparison to current and previous generations. The Internet of Things (IoT) encompasses the ubiquitous devices and innovative applications of the wireless ecosystem facilitated by them.

With increasingly mobile societies, wireless ecosystems can support many current and emerging healthcare applications. By removing position, time and other constraints, high quality wireless technologies can fulfill the vision of "Pervasive Healthcare" or healthcare to anyone, anytime, and anywhere [4]. A health monitoring infrastructure includes the many in- and on-body sensors that must relay the vital sign information they collect to a data gateway [5]. Wearable sensors [6] and wireless sensor networks [7]–[9] are intrinsic components of that infrastructure. Because antennas are the enabling technology of any wireless device, they must be designed and integrated with the sensors on flexible substrates to conform to a body and to achieve the appropriate performance characteristics that empower the communication aspects of those sensors in the body-centric and off-body wireless networks. In addition to human applications, wireless systems to monitor the structural health of civil [10], [11] and aircraft [12]–[14] structures are also extremely important.

One desirable feature of any on-body/on-surface antenna is for it to have a unidirectional pattern away from the body/surface to maximize the efficiency in either transmission or reception mode, i.e., to minimize the loss of energy in the body/structure. Electrically small broadside-radiating Huygens source antennas (HSAs) have been broadly studied in recent years due to their attractive compact size for many wireless applications and, in particular, their unidirectional radiation characteristics in the absence of any ground plane, e.g., [15]–[17]. This latter feature makes them a very interesting candidates for IoT applications associated with on-body/on-surface devices. Moreover, it has been demonstrated that their designs can be adjusted to maintain their performance characteristics even in the presence of high permittivity materials [18] as would be encountered by on-body/on-surface wireless sensors. However, the multiple-layer design of these HSAs makes their manufacturing complex and costly, and the necessary presence of vias makes attaining flexible versions quite difficult. IoT devices for health or airframe structural monitoring, for example, should be conformally mounted and, practically, should be characterized as low power and low cost [19]. Therefore, it is necessary for on-body/on-surface IoT applications to develop a unidirectional antenna that is flexible without a ground plane and that has a simple design, high radiation efficiency, and low manufacturing costs.

A single-layer, flexible, unidirectional, broadside-radiating antenna is presented in this paper. The innovative design reduces the complexity of the basic Huygens dipole antenna designs [15]–[17], where the antenna is composed of a driven electric dipole and balanced pair of near-field resonant parasitic (NFRP) dipole elements: an Egyptian axe dipole (EAD) yielding the electric dipole response and two capacitively loaded loops (CLLs) yielding the orthogonal magnetic dipole response, which produce the cardioid shape radiation associated with a HSA. These parasitic elements are printed on the different material layers, and the vias of the CLLs pierce them. Specifically, the vertical walls/vias of the CLLs are removed in the design developed in this paper; this feature allows the entire antenna to be printed on a single layer. However, without those vertical walls/vias, the parallel strips cannot achieve the loop current needed to form a magnetic dipole. Moreover, because the number of strips is small and they are not members of the infinite optical metamaterial slab configuration excited by a "plane wave" originating from a distant source [20], [21], they do not achieve a magnetic dipole response. Rather, simple parallel strip combinations can achieve an electric quadrupole,

Manuscript received August 13, 2020. This work was supported by the InnovationsFonden project of Reconfigurable Arrays for Next Generation Efficiency (RANGE) and the Global Big Data Technologies Centre, University of Technology Sydney.

R. Rodriguez-Cano is with the Antenna, Propagation and Millimeter-Wave Section (APMS) at the Department of Electronic Systems, Aalborg University, 9220 Aalborg, Denmark.

R. W. Ziolkowski is with the Global Big Data Technologies Centre, University of Technology Sydney, Ultimo NSW 2007, Australia.

Corresponding author is *Rocio Rodriguez-Cano* (e-mail: rrc@es.aau.dk)

whether they are excited by a nearby dipole or distant plane wave source, and their near-field integration with a driven dipole yields a unidirectional pattern that is not a perfect cardioid shape, but one that has a practically useful front-to-back ratio (FTBR).

Furthermore, an important new feature of 5G systems is the inclusion of millimeter-wave (mm-wave) bands and associated antennas in mobile terminals [22]–[25]. Consequently, the reported antenna has been designed for the 5G 28 GHz band at 28.475 GHz. In order to maintain consistency throughout this article, all of the simulation results reported herein were performed with the CST Studio Suite 2020. Their numerical accuracy was confirmed independently with corresponding simulations performed with the ANSYS Electromagnetics Suite v. 19.2.

The manuscript is organized as follows. Section II describes the operating principles of the developed antenna. Different designs are essayed in Section III to optimize the antenna's performance characteristics. Because of the physically small size of the design at 28.475 GHz and the lack of available resources to fabricate and measure it, a prototype was designed for operation at 1.579 GHz. Section IV describes this prototype, its testing and comparisons with its measured and simulated results. Finally, conclusions are drawn in Section V. Supplemental simulation results are included in the Appendix to provide additional theoretical details of this innovative design.

II. Operating Principle

The electric dipole is one of the most common antennas, and it has been broadly employed over the years. Its radiation pattern is maximum perpendicular to the dipole axis and has a null in that axial direction. Thus, its electric field has the well-known doughnut-shaped pattern centered about the dipole. Similarly, a magnetic dipole is readily obtained from a small loop antenna, the dipole being oriented orthogonal to the plane of the loop. It also radiates a doughnut-shaped pattern, but with its electric field being omni-directional around its axis, i.e., around the normal to the loop. Consequently, our initial attempt to achieve a via-less magnetic dipole response was to simply use the magnetic dipole antenna arising from the Huygens dipole antenna design in [15], remove the EAD NFRP element, and then remove all four vias of the CLL NFRP elements. It was anticipated that this would be successful because of the vaunted first magnetic optical metamaterial based on two parallel conducting strips [20], a concept that has been extended recently to attain a matched zero refractive index metasurface in the terahertz band [21]. However, it was unsuccessful for the following reasons.

Consider the continuous wave (CW) electric elemental current source driven with the frequency $f = \omega/2\pi$ and located at the point $\vec{r}_0 = x_0\,\hat{x} + y_0\,\hat{y} + z_0\,\hat{z}$ and oriented along the $+x$-direction:

$$\vec{J} = I_e(\omega)\ell_e\,\delta(x-x_0)\,\delta(y-y_0)\,\delta(z-z_0)\,\hat{x} \tag{1}$$

where $I_e\ell_e$ represents the electric current moment with units $A-m$. It is straightforward to show that the electromagnetic fields in the far field of this source referenced to the coordinate origin are:

$$\vec{E}^{ff}_{\omega,J} = +j\,\omega\,\mu\,I_e(\omega)\ell_e\,\frac{e^{-jkr}}{4\,\pi\,r}\,e^{+j\,k\,\hat{r}\cdot\vec{r}_0}\;(\,\hat{r}\times\hat{r}\times\hat{x}\,)$$
$$\vec{H}^{ff}_{\omega,J}(\vec{r}) = \frac{1}{\eta}\,\Big[\,\hat{r}\times\vec{E}^{ff}_{\omega,J}(\vec{r})\,\Big] \tag{2}$$

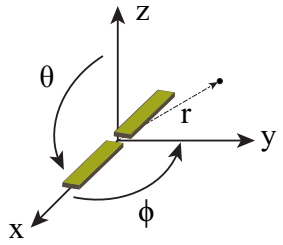

Fig. 1. Dipole oriented along the x-axis and centered at the origin of the coordinate system.

Consider the x-oriented dipole centered at the origin, i.e., $\vec{r}_0 = 0$, shown in Fig. 1. Since

$$\hat{r}\times\hat{x} = \sin\phi\,\hat{\theta} + \cos\theta\cos\phi\,\hat{\phi}$$
$$\hat{r}\times\hat{r}\times\hat{x} = -\cos\theta\cos\phi\,\hat{\theta} + \sin\phi\,\hat{\phi} \tag{3}$$

the electric field takes the form

$$\vec{E}^{ff}_{\omega,J} = +j\,\omega\,\mu\,I_e(\omega)\ell_e\,\frac{e^{-jkr}}{4\,\pi\,r}\,\vec{\mathcal{P}}_{\rm element}(\theta,\phi) \tag{4}$$

where the element vector pattern is

$$\vec{\mathcal{P}}_{\rm element}(\theta,\phi) = -\cos\theta\cos\phi\,\hat{\theta} + \sin\phi\,\hat{\phi} \tag{5}$$

Along the x-axis where $(\theta=\pi/2, \phi=0,\pi)$, the electric field is clearly zero. In the zx-plane where $\phi=0$, the pattern has the figure-eight form, $\cos\theta$, with its maximum along the z-axis where $\theta=0,\pi$. In the yz-plane where $\phi=\pi/2, 3\pi/2$, the pattern is omni-directional. Note that the electric field vector along the $+z$ axis with $(\theta=0, \phi=0)$ is proportional to $-\hat{\theta} = +\hat{x}$ and along the $-z$ axis with $(\theta=\pi, \phi=0)$ is proportional to $\hat{\theta} = +\hat{x}$.

Now consider two such dipoles, each displaced symmetrically about the x-axis a distance $d_z/2$ along the z axis from it and with the top (bottom) one having its current moment along the $+x$-axis ($-x$-axis). Since $\hat{r}\cdot\hat{z} = \cos\theta$, the total far-field electric field takes the form

$$\vec{E}^{ff}_{\omega,J} = +j\,\omega\,\mu\,I_e(\omega)\ell_e\,\frac{e^{-jkr}}{4\,\pi\,r}\,\vec{\mathcal{P}}_{\rm total}(\theta,\phi) \tag{6}$$

where the total vector pattern is the product of the array pattern and element vector pattern:

$$\vec{\mathcal{P}}_{\rm total}(\theta,\phi) = \mathcal{P}_{\rm array}(\theta,\phi)\ \vec{\mathcal{P}}_{\rm element}(\theta,\phi) \tag{7}$$

and the array pattern is simply

$$\begin{aligned}\mathcal{P}_{\rm array,z}(\theta,\phi) &= e^{+j\,(kd_z/2)\,\cos\theta} - e^{-j\,(kd_z/2)\,\cos\theta} \\ &= 2j\ \sin\left[\left(\frac{kd_z}{2}\right)\cos\theta\right]. \end{aligned}\tag{8}$$

With the electrical distance kd_z being small, the array pattern is proportional to $\cos\theta$ and the normalized total vector pattern extracted from $\mathcal{P}_{\rm array,z}\vec{\mathcal{P}}_{\rm element}$ becomes

$$\vec{\mathcal{P}}_{\rm tot,norm}(\theta,\phi) = -\cos^2\theta\cos\phi\,\hat{\theta} + \cos\theta\sin\phi\,\hat{\phi}. \tag{9}$$

The change is primarily in the yz-plane because the overall pattern is now proportional to $\cos\theta$, i.e., it yields a null along the entire xy-plane – not simply a null along the y axis.

Note that the electric field of a magnetic dipole oriented along the y axis would have its doughnut pattern centered along it. Its null would be only along the y axis. In contrast, the two closely spaced electric dipoles with opposite moments radiate a quadrupole pattern with a null along the entire xy-plane, i.e., they represent a quadrupole radiator [26], [27], not a magnetic dipole. In fact, the total pattern is proportional to the associated Legendre polynomial $P_2^2(\cos\theta)$ in the zx-plane ($\phi = 0$), one of the possible quadrupole terms in a multipole expansion. Nevertheless, note that the orientation of the electric field along the $+z$ axis is proportional to $-\hat{\theta} = +\hat{x}$ and along the $-z$ axis is proportional to $-\hat{\theta} = -\hat{x}$. Consequently, if the amplitude of the field radiated by this quadrupole antenna was strong enough, it could in principle cancel the backlobe of a dipole antenna. Unfortunately, as expected, the quadrupole response was weaker than the dipolar one when the strips were taken to be parasitic elements. Consequently, it was decided to try two pairs of dipoles with current moments similar to those realized on the CLL NFRP elements.

Therefore, if one had a pair of quadrupole radiators oriented with the current moment directions of one pair of dipoles being the same as the other and displaced symmetrically along the y-axis at a distance $d_y/2$, the additional array pattern ($\hat{r}\cdot\hat{y} = \sin\theta\sin\phi$) is

$$\mathcal{P}^{same}_{\rm array,y}(\theta,\phi) = 2\cos\left[\left(\frac{kd_y}{2}\right)\sin\theta\sin\phi\right] \tag{10}$$

With kd_y being small and $\cos(\xi) \simeq 1$ and $\sin(\xi) \simeq \xi$ for $\xi \ll 1$, the pattern in the yz-plane retains the same quadrupolar form as the single pair of strips. This arrangement does indeed boost the total radiated power of the quadrupole field.

On the other hand, if the dipole pair positioned along the $-y$ axis is oriented opposite to the original pair positioned along the $+y$ axis, the additional array pattern becomes

$$\mathcal{P}^{opposite}_{\rm array,y}(\theta,\phi) = 2j\sin\left[\left(\frac{kd_y}{2}\right)\sin\theta\sin\phi\right] \tag{11}$$

The total vector pattern is proportional to $\mathcal{P}^{opposite}_{array,y}\ \mathcal{P}_{array,z}\ \vec{\mathcal{P}}_{element}$; and with kd_y being small, one obtains:

$$\begin{aligned}\vec{\mathcal{P}}_{\rm total,norm}(\theta,\phi) &= \sin\theta\cos\theta\sin\phi \\ &\times\left(\cos\theta\cos\phi\,\hat{\theta} - \sin\phi\,\hat{\phi}\right)\end{aligned}\tag{12}$$

The pattern has two null planes: $\phi = 0$ (zx-plane) and $\theta = \pi/2$ (xy-plane). This behavior would not be beneficial to the desired outcome because of the additional null introduced, notably the one along the entire zx-plane. Note that the total pattern is proportional to the associated Legendre polynomial $P_2^1(\cos\theta)$, another quadrupole term.

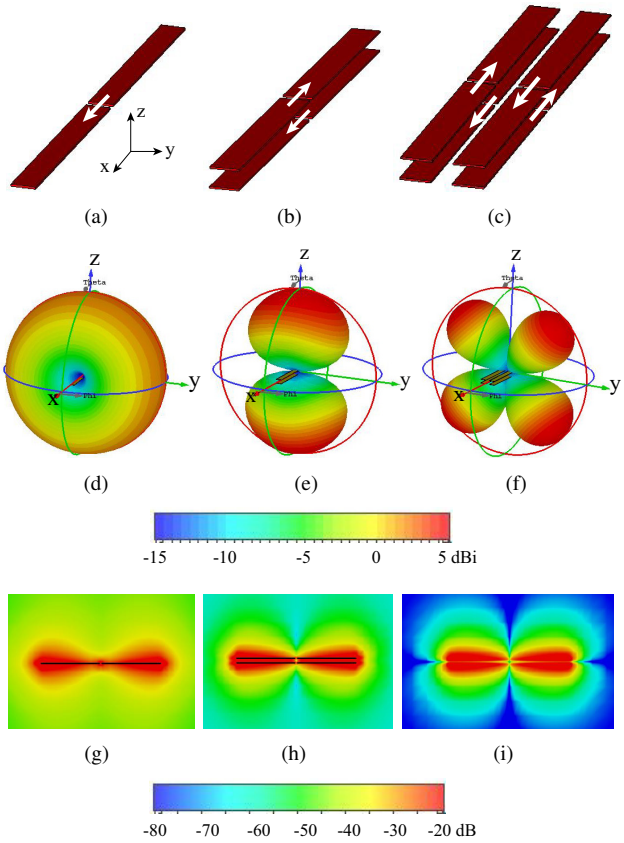

Fig. 2. The white arrows represent the direction of the feeding port. (a) Electric dipole. (b) Pair of dipoles. (c) Two pairs of dipoles. 3D directivity patterns: (d) of (a), (e) of (b), and (f) of (c). Electric field distribution in the zx-plane (g) of (a), (h) of (b), and (i) of (c).

This analysis was confirmed with CST simulations of the dipole elements shown in Figs. 2(a)-(c). The models consisted of copper strips whose lengths along the x axis were 4.686, 4.86 and 4.9 mm, i.e., $0.444\lambda_0$, $0.461\lambda_0$ and $0.465\lambda_0$, respectively, to make them resonant at 28.475. The width along the y axis was 0.3 mm ($0.028\lambda_0$), and the thickness along the z axis was 0.018 mm ($0.0017\lambda_0$). These strips were excited

at 28.475 GHz ($\lambda_0 = 10.53$ mm) with ideal current sources centered in 0.1 mm ($0.0095\lambda_0$) gaps in the middle of the strips with the indicated current directions (black arrows). The strip pairs in Figs. 2(b) and 2(c) were separated by 0.182 mm ($0.0173\lambda_0$) in the z direction. The two pairs of strips shown in Fig. 2(c) were separated by 0.2 mm ($0.019\lambda_0$) in the y direction. The corresponding simulated far-field patterns are given in Figs. 2(d)-(f); the associated near-field electric field distributions are presented in Figs. 2(g)-(i). The dipole pattern in Fig. 2(d) has the predicted null along the x axis; the quadrupolar pattern (having the P_2^2 form) being null along the xy-plane is recovered in Fig. 2(e), and the quadrupolar pattern (having the P_2^1 form) with its nulls along the xy and zx planes is confirmed in Fig. 2(f). The respective maximum directivity of the patterns in Figs. 2(g)-(i) are 2.07, 6.07 and 6.69 dBi, respectively. The plane wave scattering problem corresponding to the geometry in Fig. 2(b) is considered in Appendix A. The results also exhibit the quadrupolar pattern shown in Fig. 2(e).

While the analytical results suggested that a combination of an excited dipole and two pairs of NFRP strips could yield some sort of unidirectional pattern, a typical quasi-Yagi antenna, i.e., a configuration with one driven printed dipole (in red) and one parasitic strip parallel to it (in green), was also considered. This configuration is illustrated in Fig. 3(a). The excitation frequency was again 28.475 GHz. The current exciting the active dipole has the same orientation as the one in Fig. 2(a). The induced current on the parasitic strip is oppositely oriented like the configuration in Fig. 2(b). The simulated 3D radiation patterns at 28.475 GHz for the cases in which the dipole lengths are much smaller than the excitation wavelength, 11.1 mm, and near to half that wavelength are shown in Figs. 3(b) and 3(c), respectively. In particular, the dipole length in the first case was 2.1 mm and 4.92 mm in the latter case. The width of the strips was the same as those in Fig. 2, i.e., 0.3 mm. The separation of the strips was again 0.182 mm in the z direction.

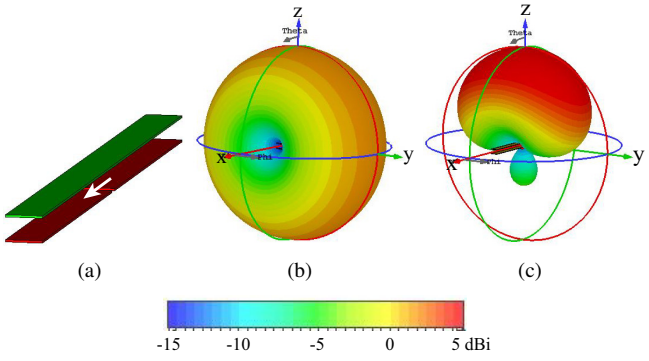

Fig. 3. Quasi-Yagi system. (a) Simulation model of the two parallel elements, one driven (red) and one parasitic element (green). Directivity pattern for the element lengths: (b) $\ll \lambda/2$, and (c) $\sim \lambda/2$.

One immediately sees in Fig. 3 that the shape of the directivity pattern depends critically on the length of the elements. If they are much smaller than $\lambda/2$, the directivity pattern is the typical doughnut-shaped electric dipole one. On the other hand, when their length becomes closer to $\lambda/2$ with a small separation, a more directive pattern is obtained. The minimum separation of the driven and parasitic dipoles to obtain a directive pattern in this latter case was 0.098 mm, approximately $\lambda_{res}/100$. The doughnut-shaped pattern in Fig. 3(b) for the very short strip case has a peak directivity of 1.95 dBi. The unidirectional pattern in Fig. 3(c) for the half-wavelength case has a maximum directivity of 7.25 dBi and a FTBR of 11.3 dB.

The effects on the patterns caused by the separation of the driven and parasitic elements when they are $\sim \lambda/2$ in size were also considered. The doughnut-shaped directivity pattern in Fig. 3(b) was produced again when the elements were placed very close to each other, i.e., for a separation distance of only 0.002 mm. A slightly larger maximum directivity of 2.65 dBi was obtained in comparison to that shorter-element case. The unidirectional directivity pattern in Fig. 3(c) was obtained when the element separation was 0.0182 mm. The maximum directivity was again 7.25 dBi and the FTBR was 11.3 dB. Note that this maximum directivity is nearly 2.5 dB more than what one would obtain for an ideal Huygens dipole source, 4.77 dBi. Nevertheless, the realized gain is only -5.42 dBi because the antenna is very poorly matched to the source, with $|S_{11}|_{min}$ being only -0.4 dB. The reason for the large reflection coefficient despite the size of the elements is that the opposite, closely spaced currents cancel each other out yielding a very small resistive part of the input impedance. Also, as another consequence, the total radiated power is quite low.

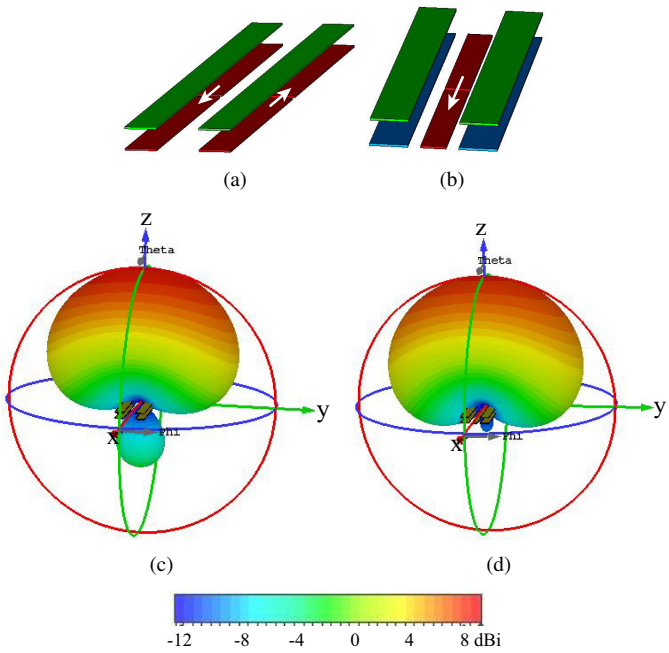

Fig. 4. Comparison models. (a) Two pairs of parallel dipoles, with the bottom ones as driven elements (red), and the top ones as parasitic (green). (b) One driven element (red) and 4 parasitic strips (green and blue). (c) Directivity radiation pattern of (a). (d) Directivity radiation pattern of (b).

With these analytical and numerical results in hand, it was decided to investigate different combinations of driven dipoles and parallel parasitic strips to achieve the desired single-layer, unidirectional antenna with good maximum directivity and

FTBR values. The models of two representative cases are shown in Fig. 4. The model in Fig. 4(a) has two pairs of dipoles with only the bottom ones being active (in red) and the top ones being parasitics (in green). The separation between the active and passive elements is 0.182 mm ($0.0173\lambda_0$) and between the two pairs is 0.4 mm ($0.038\lambda_0$). The length and width of the driven elements are 4.86 mm and 0.3 mm ($0.4613\lambda_0$ and $0.0285\lambda_0$), respectively. The directivity pattern has a peak value of 7.53 dBi in the $+z$ direction, but has a large back lobe yielding a FTBR of only 7.7 dB. Moreover, the realized gain is small at -3.78 dBi because of the same current-cancellation issue associated with the single pair of elements in Fig. 3.

In contrast, the model in Fig. 4(b) has only one driven element (in red) and has two pairs of parasitic strips (in green and blue). The driven element is centered between the two parasitic pairs. The elements of each pair are again separated by 0.182 mm ($0.0173\lambda_0$) and the pairs are again separated by 0.4 mm ($0.038\lambda_0$). The length and width of the driven element are 4.84 mm and 0.2 mm ($0.459\lambda_0$ and $0.019\lambda_0$), respectively. The length and width of the parasitic strips are 4.84 mm and 0.3 mm ($0.459\lambda_0$ and $0.0285\lambda_0$), respectively. This configuration is analogous to the one discussed in relation to (10). While the peak directivity in the broadside direction of the one-driven, four-parasitic model is slightly smaller, 7.04 dBi, than the two active – two parasitic case, the FTBR has significantly improved. Its maximum value is now 15.1 dB. This pattern is clearly much closer to the desired cardiod shape produced by a broadside-radiating Huygens dipole antenna.

III. Trial and Optimized Designs and Their Simulated Performance Characteristics

After achieving a structure with the desired radiation pattern, the impacts on the performance of the design were assessed when its structural parameters were varied. Parameter studies dealing with asymmetric strip designs, offsets of the strips on one layer with respect to the other, and interdigitation of the driven dipole were considered. The final optimized design was obtained based on these comprehensive simulation series.

A. Trial Designs

A variety of trial designs based on the ideal simulation model in Fig. 4(b) were explored to develop a version matched to a 50-Ω source at the desired resonance frequency, 28.475 GHz, that attains the desired unidirectional broadside radiation performance characteristics. The resulting electric quadrupole systems are composed of 4 NFRP strips, two printed on the top surface and two printed on the bottom surface of a substrate. The substrate is Rogers Duroid^{TM} 5870 with a dielectric constant 2.33 and a 0.0009 loss tangent. Its length and width are 4.86 mm and 1.67 mm ($0.4613\lambda_0$ and $0.1585\lambda_0$), respectively. Its thickness is 0.254 mm ($0.0241\lambda_0$). The driven dipole is printed on the bottom surface and centered between all of the parasitic strips. The resonance frequencies of these trial designs are all in the neighborhood of the target frequency.

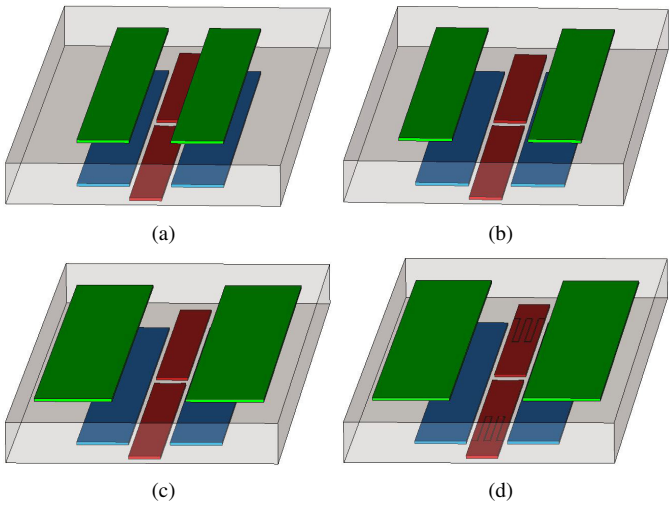

Fig. 5. Electric quadrupole designs. Driven elements in red; parasitic elements in green and blue. (a) Model A. (b) Model B. (c) Model C. (d) Model D.

The front and top views of different combinations of the parasitic and driven elements are illustrated in Fig. 5. In all cases the driven dipole element is excited with a 50-Ω coaxial feedline. The corresponding reflection coefficients and realized gain patterns of all of these models are plotted in Figs. 6 and 7, respectively. The variable parameters in the legend are w, the width of the parasitic strips, and d, the offset to the driven dipole. The subscripts t and b represent top and bottom.

Model A, Fig. 5(a), has the top and bottom parasitic strips centered above each other with the same lengths and widths, respectively, 3.476 and 0.32 mm ($0.329\lambda_0$ and $0.0304\lambda_0$). They are offset 0.13 mm ($0.0123\lambda_0$) along the y-axis from the center. The input impedance of Model A at its resonance frequency is $80\ \Omega$. It differs from the target $50\ \Omega$ which causes the minimum $|S_{11}|$ value in Fig. 6 to only be about -15 dB.

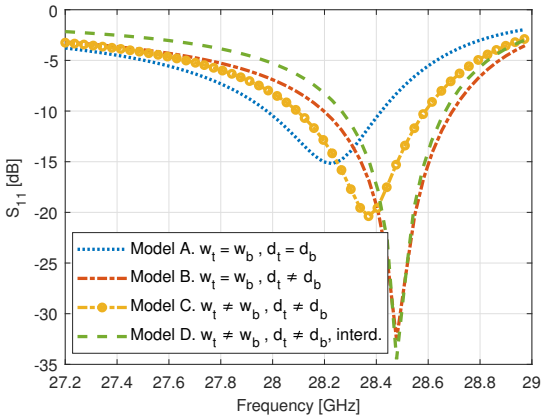

Fig. 6. Reflection coefficient comparisons of the trial quadrupole designs as functions of the source frequency. Curve (a): strip widths are $w_t = w_b = 0.0304\lambda_0$ and offset distances are $d_t = d_b = 0.0028\lambda_0$. Curve (b): widths are $w_t = w_b = 0.0304\lambda_0$, and offsets are $d_t = 0.0123\lambda_0$, $d_b = 0.0028\lambda_0$. Curve (c): widths are $w_t = 0.0456\lambda_0$, $w_b = 0.0304\lambda_0$, and offsets are $d_t = 0.0123\lambda_0$, $d_b = 0.0028\lambda_0$. Curve (d): the same dimensions as Curve (c), but the driven dipole is interdigitated.

Model B, Fig. 5(b), simply offsets those top strips by

0.1 mm ($0.0095\lambda_0$) y-axis towards the outside edges of the substrate with respect to the previous model. This does reduce the impedance value at its resonance frequency and, hence, improves the minimum $|S_{11}|$ value to below -20 dB as seen in Fig. 6. Model C, Fig. 5(c), is the same as Model B but with the widths of the top strips increased by 0.16 mm ($0.0152\lambda_0$) along the y-axis towards the outside edges of the substrate. This modification again improves the impedance match with the minimum $|S_{11}|$ value now below -30 dB and approximately at the target frequency as seen in Fig. 6. Model D is the same as Model C but with the driven element modified to have two interdigitated capacitors embedded in it. The resonance frequency is at the target frequency and the $|S_{11}|_{min}$ value has been improved a bit further. The interdigitated dipole element greatly facilitated the impedance matching in the final design which includes the actual feed structure.

While the 2D realized gain patterns in the yz plane of all of the cases shown in Fig. 7 are similar, each evolutionary stage of these trial designs tweaked up the peak realized gain and FTBR values a little more. For instance, Model C exhibits a slight increase of the peak realized gain from 4.72 to 4.8 dBi and of the FTBR from 8.8 to 9.3 dB in comparison to Model B. In the final design, Model D, the interdigitated dipole further increments the realized gain to 4.85 dBi and the FTBR to 9.4 dB.

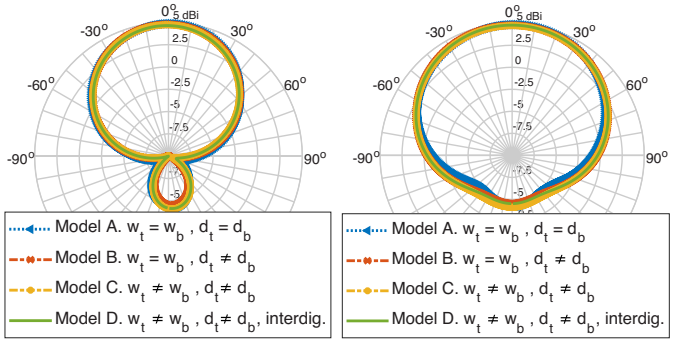

(a) (b)

Fig. 7. 2D realized gain pattern comparisons of the trial quadrupolar designs as functions of the source frequency. (a) $\phi = 0°$. (b) $\phi = 90°$.

B. Optimized Design

The best unidirectional quadrupole trial design, Model D with its coax feedline excitation, was then selected and optimized. The geometry and the design parameters of the optimized antenna are illustrated in Fig. 8. The substrate and its dimensions are the same as those in Models A-D, i.e., Rogers 5870 and 4.86 mm $\times$1.67 mm $\times$0.254 mm ($0.45\lambda_0 \times 0.15\lambda_0 \times 0.02\lambda_0$). These dimensions give $ka = 1.23$, where a is basically the distance from the center of the substrate to a corner given its thinness. The bright green regions in Figs. 8(a) and 8(b) indicate the copper strips on the top surface. The light blue regions are the parasitic copper traces and the red region is the driven dipole on the bottom surface. The coax feedline is visible in Fig. 8(c) and the outlines of its center and outer conductors are readily seen in Figs. 8(a) and 8(b). The corresponding optimized design parameters are given in Table I.

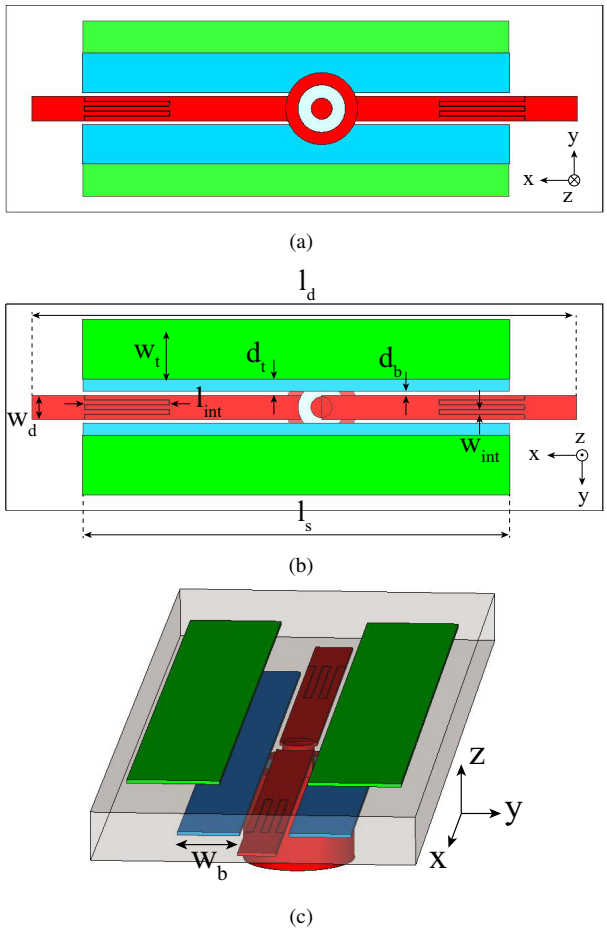

Fig. 8. CST simulation model used to optimize the quadrupole antenna design. (a) Bottom view. (b) Top view. (c) 3D isometric view. Driven elements in red; parasitic elements in green and blue.

TABLE I
FINAL DESIGN PARAMETERS OF THE 28.475 GHZ UNIDIRECTIONAL QUADRUPOLE ANTENNA (DIMENSIONS IN MILLIMETERS (MM))

l_d	w_d	l_s	w_t	d_t	w_b	d_b	l_{int}	w_{int}
4.44	0.196	3.47	0.48	0.13	0.32	0.029	0.69	0.044

C. Simulated Performance Characteristics

The CST simulated reflection coefficients of the quadrupole antenna are presented in Fig. 9. It is well-matched to the source with the $|S_{11}|$ values being less than –10 dB, from 28.25 to 28.65 GHz (400 MHz). The –10-dB fractional bandwidth is thus 1.4%. The corresponding –3 dB bandwidth is 1.22 GHz, which gives a fractional bandwidth of 4.2%.

The input impedances of these antennas are also given in Fig. 9. The resonance frequency is 28.475 GHz. Its input impedance at that frequency is $49.4 + j0.57\ \Omega$, which explains the $|S_{11}|_{min}$ value being less than –35 dB. Fig. 10 shows the realized gain patterns of the antenna in the two primary vertical planes, $\phi = 0°$ and $\phi = 90°$. It clearly shows that the antenna radiates a cardioid pattern with its maximum in the direction

broadside to the plane of the antenna. The realized gain at the resonance frequency is 4.85 dBi, which is more than double the gain of the half-wave dipole and is greater than the ideal Huygens source value, 4.77 dBi. The FTBR is 9.4 dB. The total efficiency of the antenna is 85%.

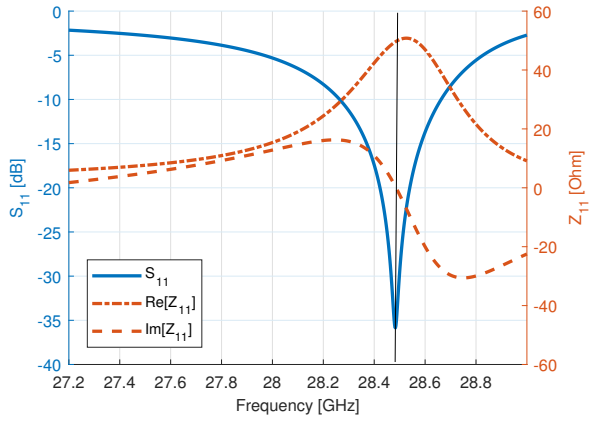

Fig. 9. Reflection coefficient and input impedance of the optimized quadrupole antenna as a function of the source frequency.

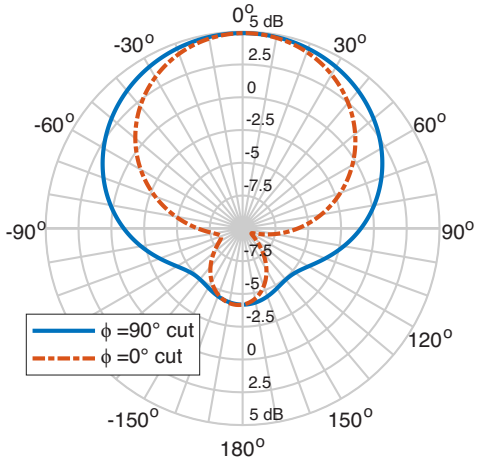

Fig. 10. 2D realized gain pattern in the zx and yz planes of the optimized quadrupole antenna at its resonance frequency, 28.475 GHz.

IV. Results of the 1.579 GHz Proof-of-Concept Prototype

Due to the quite small size of the designed 28 GHz band antenna, 4.86 mm $\times$1.67 mm, an easier to fabricate and measure prototype was designed and manufactured for operation in the L-band near the GPS-L1 frequency, 1575.42 MHz (190.29 mm wavelength). This frequency was selected because if the design was successfully verified, the prototype would be proven useful for some GPS-L1 related applications.

Since the resonance frequency was reduced significantly, a simple scaling of the structure was insufficient to attain the prototype design. The Rogers Duroid^{TM} 5880 substrate was employed; its dielectric constant and loss tangent are $\epsilon_r = 2.2$ and 0.0009, respectively. The thickness of the substrate, 1.575 mm ($0.0084\lambda_0$), was selected for ease of handling. The optimized design parameters are listed in Table II. The optimized design has the resonance frequency, 1.579 GHz ($\lambda_0 = 187.61$ mm). The overall dimensions of the fabricated prototype were 98.25 mm $\times$ 37.60 mm ($0.52\lambda_0 \times 0.20\lambda_0$) giving $ka = 1.74$, where a is the radius of the smallest sphere that contains the entire structure.

TABLE II
Final Design Parameters of the 1.579 GHz Unidirectional Quadrupole Prototype (Dimensions in Millimeters (mm))

l_d	w_d	l_s	w_t	d_t	w_b	d_b	l_{int}	w_{int}
84.0	4.03	65.6	9.0	0.736	6.0	0.486	10.0	1.0

A picture of the prototype is shown in Fig. 11. A differential feed structure was chosen for the measurements instead of the single coax-feed inherent in the 28.475 GHz design. This differential choice eliminated the need for any baluns and considerably reduced the possible radiation emissions from the common mode currents [28]. The two coaxial cables were soldered together on their outer conductors, as can be seen. The driven dipole element in the corresponding simulated design was excited with a 50-Ω discrete port to ensure a fair comparison.

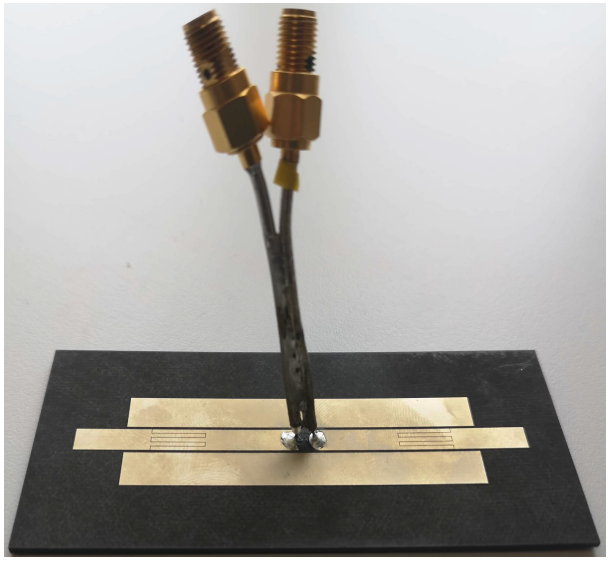

Fig. 11. View of the bottom of the prototype quadrupole antenna with the differential feed attached. The two outer conductors of the coaxial cables are soldered together as required.

The experimental methodology for the characterization of the impedance of balanced antennas given in [29] was employed to extract the reflection coefficient of the measured prototype. The differential input impedance can be obtained directly from the measured S-parameters as follows:

$$Z_{\text{diff}} = \frac{2Z_0(1 - S_{11}S_{22} + S_{12}S_{21} - S_{12} - S_{21})}{(1 - S_{11})(1 - S_{22}) - S_{21}S_{12}}. \quad (13)$$

The corresponding reflection coefficient is calculated as

$$|S_{11}| = \left| \frac{Z_{\text{diff}} - Z_0}{Z_{\text{diff}} + Z_0} \right|. \quad (14)$$

After obtaining the S_{11} values, the calculation of the input impedance is straightforward.

A dipole representation of the actual measurement system configuration is depicted in Fig. 12. Each of the ports of the dipole is connected through a measurement jig to one of the ports of the VNA. To deembed the influence of the jig, the calibration plane is shifted through the port extension technique.

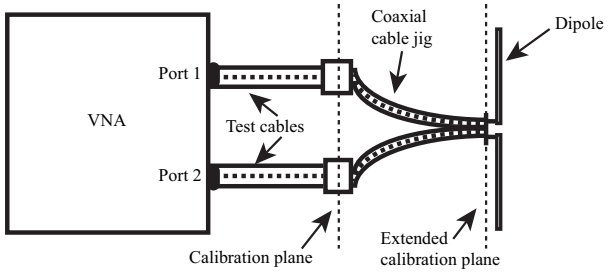

Fig. 12. Representation of the differential-feed measurement setup to obtain the S-parameters.

The measured reflection coefficient results, together with their corresponding simulated values, are shown in Fig. 13. There was a slight frequency blueshift, 12.9 MHz (0.81%), in the measured resonance frequency from 1.579 GHz. It arose from slight fabrication errors and the differential-feed connection issues. This was confirmed with further simulations. In particular, with the dimensions of the quadrupole along the x-axis shrunk by 0.49% in the simulation model, the same resonance frequency as the measured prototype is obtained.

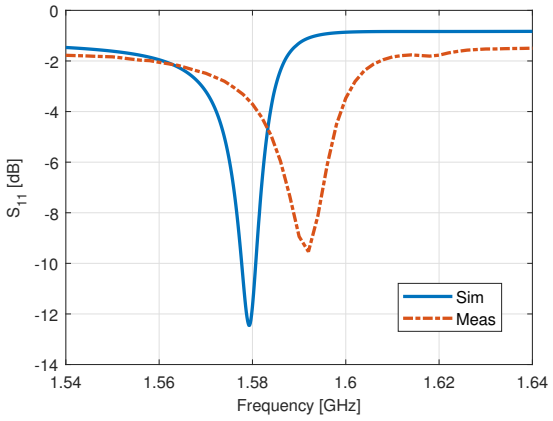

Fig. 13. Measured and simulated reflection coefficients of the quadrupole prototype as functions of the source frequency.

The measured and simulated input impedances of the quadrupole prototype obtained from the reflection coefficients are compared in Fig. 14. Reasonable agreement between the measured and simulated values is observed. The simulated input impedance at the resonance frequency was $30.84+j2.22\ \Omega$ and the measured one was $25.04 + j2.06\ \Omega$.

The realized gain pattern measurements were obtained in a Satimo near-field range as shown in Fig. 15. A 180° hybrid coupler was connected to the differential-feed of the prototype to guarantee that the currents in both arms of the feed have

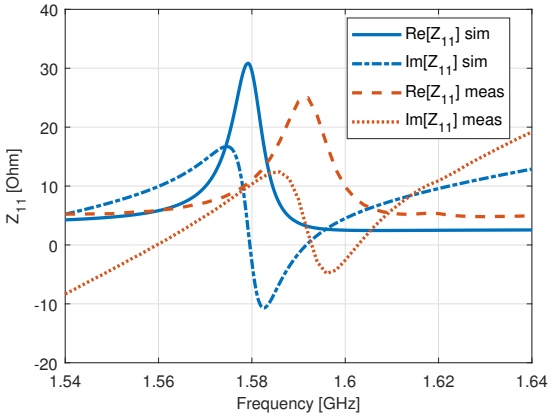

Fig. 14. Measured and simulated input impedance values of the quadrupole prototype as functions of the source frequency.

the same magnitude, but opposite direction. The measured and simulated realized gain patterns in the two principal vertical planes are compared in Fig. 16. The peak realized gain was measured at the resonant frequency; it reached 3.5 dBi in both planes. The FTBR values were 9.69 dB and 5.45 dB in the $\phi = 0°$ and $\phi = 90°$ planes, respectively. The measured results show quite good agreement with their simulated ones. They confirm the unidirectional, broadside-radiating performance of the prototype.

Fig. 15. Prototype quadrupole antenna as the antenna under test (AUT) in the anechoic chamber for measurement of its realized gain patterns and total efficiency.

The total efficiency of the prototype was simulated and then also measured with the Satimo near-field range by obtaining the total radiated power. These results are compared in Fig. 17. The simulated total efficiency at the resonance frequency is 64.27%, while the measured value was 51.89%. The measured value is smaller not only due to the poorer impedance match exhibited by the prototype as shown in Fig. 13, but also from the fact that the simulation model did not reproduce the exact details of the differential feed shown in Fig. 11. The actual feed structure and how it was mounted on the antenna simply introduced additional losses. Not only do these simulation,

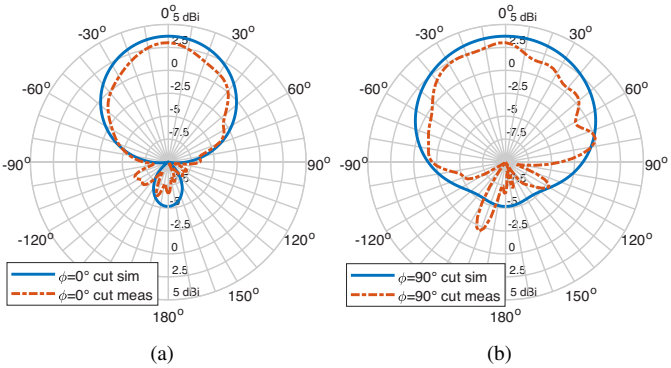

(a) (b)

Fig. 16. Measured and simulated realized gain patterns of the quadrupole prototype at 1.579 GHz. (a) $\phi = 0°$. (b) $\phi = 90°$.

fabrication, assembly and measurement issues exacerbate the differences between the simulation model and measured results of the prototype, but also the noticeable differences between the 1.579 GHz performance and that of the 28.475 GHz design.

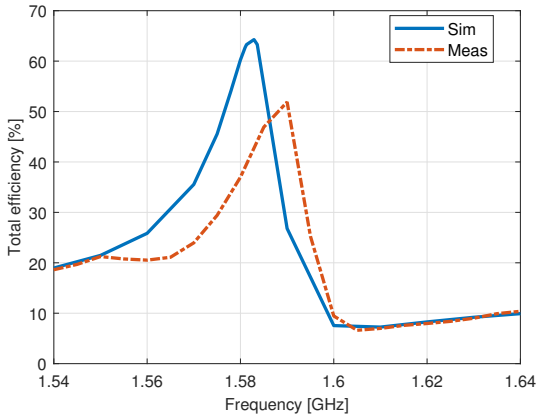

Fig. 17. Measured and simulated total efficiency of the quadrupole antenna as functions of the source frequency.

V. Conclusion

An innovative single-layer, unidirectional, broadside-radiating quadrupole antenna was developed for operation at 28.475 GHz in the 5G 28 GHz band for potential on-body/on-surface IoT applications. It consists of a driven dipole and two pairs of NFRP elements printed on a single substrate layer. The dimensions and locations of its parasitic and driven elements were assessed. The single layer design is much simpler than many of the recently reported multilayered broadside-radiating Huygens dipole antennas. The parameter studies used to determine the optimized arrangement of the driven and NFRP elements were discussed. The quadrupole nature of the antenna was demonstrated analytically and numerically. It was explained how this antenna system produces cardioid-shaped realized gain patterns when the lengths of its parasitic strips are close to half a wavelength.

A proof-of-principle prototype was fabricated and tested at the more manageable frequency of 1.579 GHz. Its size was much easier to handle and the available fabrication and measurement facilities readily accommodated it. A differential-feed was introduced for the measurements of the prototype rather than the single coaxial-feed structure in the 28 GHz design. It eliminated the impact of any cable leakage currents on the measured results. The measured and simulated unidirectional, broadside radiating results were confirmed and demonstrated to be in good agreement. While the 28 GHz band design is attractive for 5G IoT applications, the validated prototype may also prove useful for GPS-L1 systems. The many potential on-body/on-surface IoT applications to which this system could be applied require their antennas to be conformal. Preliminary simulation results have demonstrated that the 28 GHz quadrupole antenna system maintains the attractive radiation properties realized in its planar state in both its longitudinal and transverse bent states adding further merit to its innovative design.

Acknowledgments

The authors would like to thank Kim Olesen and Kristian Banks for their help in the manufacturing and measurement of the prototype antenna.

The authors would like to thank Distinguished Professor and Head of the Global Big Data Technologies Centre at the University of Technology Sydney, Jay Guo, for hosting RRC as a Visiting Scholar to work with RWZ for a month at the end of 2019. The concepts described in this article originated during that UTS visit.

Appendix A
Two Passive Strips with Plane Wave Excitation

Because of the innovative aspects of the reported quadrupolar design, many additional checks on the analysis and its outcomes were considered. In particular, the quadrupolar behavior obtained with the active dipole and parasitic strip in Fig. 2(b) was assessed with a plane wave excitation of the equivalent two passive strip configuration, i.e., with them as scatterers. This model represents one unit cell of the infinite metasurface constructs considered in [20], [21]. Since the electric quadrupolar response was realized in the finite antenna design rather than a magnetic dipole one upon which those works were based, quadrupolar scattering results would also represent an additional contribution, i.e., one to the fundamental understanding of how finite electromagnetic metastructure designs actually work.

This simulation model is shown in Fig. 18(a). The incident plane wave is propagating along the $+z$ axis. Its electric field is oriented along the strips in the $+x$ direction and its magnetic field is orthogonal to the surface between the strips in the $+y$ direction. The simulated 2D directivity patterns of the scattered field are shown in Fig. 18(b) in the vertical zx-plane and the horizontal xy-plane. Their shape is a slightly asymmetric version of the quadrupolar form in Fig. 2(e). The asymmetry arises because the induced currents on both strips do not have the same magnitude. The 3D pattern is null along the entire xy-plane. These results confirm the quadrupolar response irrespective of the source type.

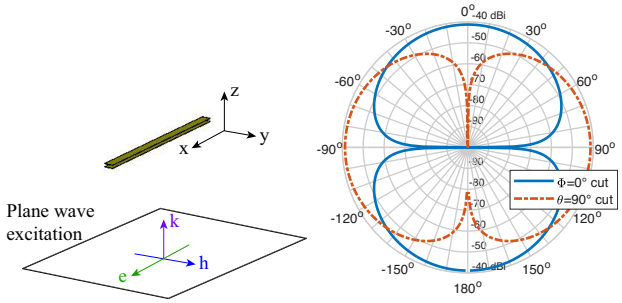

(a) (b)

Fig. 18. Two parallel copper strips excited by a plane wave. (a) Simulation model. (b) 2D RCS directivity patterns in the zx-plane (blue) and xy-plane (red) at 28.475 GHz.

REFERENCES

[1] L. Chettri and R. Bera, "A comprehensive survey on Internet of Things (IoT) toward 5G wireless systems," *IEEE Internet Things J.*, vol. 7, no. 1, pp. 16–32, Jan. 2020.

[2] M. R. Palattella, M. Dohler, A. Grieco, G. Rizzo, J. Torsner, T. Engel, and L. Ladid, "Internet of Things in the 5G era: Enablers, architecture, and business models," *IEEE J. Sel. Areas Commun.*, vol. 34, no. 3, pp. 510–527, Mar. 2016.

[3] K. Shafique, B. A. Khawaja, F. Sabir, S. Qazi, and M. Mustaqim, "Internet of Things (IoT) for next-generation smart systems: A review of current challenges, future trends and prospects for emerging 5G-IoT scenarios," *IEEE Access*, vol. 8, pp. 23 022–23 040, 2020.

[4] U. Varshney, "Pervasive healthcare and wireless health monitoring," *Mobile Netw. Appl.*, vol. 12, no. 2-3, pp. 113–127, Jul. 2007.

[5] T. Yilmaz, R. Foster, and Y. Hao, "Detecting vital signs with wearable wireless sensors," *Sensors*, vol. 10, no. 12, pp. 10 837–10 862, Dec. 2010.

[6] P. J. Soh, G. A. Vandenbosch, M. Mercuri, and D. M.-P. Schreurs, "Wearable wireless health monitoring: Current developments, challenges, and future trends," *IEEE Microw. Mag.*, vol. 16, no. 4, pp. 55–70, Apr. 2015.

[7] Y. Hao and R. Foster, "Wireless body sensor networks for health-monitoring applications," *Physiol. Meas.*, vol. 29, no. 11, p. R27, Oct. 2008.

[8] P. S. Hall and Y. Hao, Eds., *Antennas and Propagation for Body-Centric Wireless Communications*, 2nd ed. Norwood, MA: Artech house, 2012.

[9] C. C. Poon, B. P. Lo, M. R. Yuce, A. Alomainy, and Y. Hao, "Body sensor networks: In the era of big data and beyond," *IEEE Rev. Biomed. Eng.*, vol. 8, pp. 4–16, Apr. 2015.

[10] J. P. Lynch, "An overview of wireless structural health monitoring for civil structures," *Philos. Trans. Royal Soc. A*, vol. 365, no. 1851, pp. 345–372, Dec. 2007.

[11] Y. Wang, J. P. Lynch, and K. H. Law, "A wireless structural health monitoring system with multithreaded sensing devices: Design and validation," *Struct. Infrastructure Eng.*, vol. 3, no. 2, pp. 103–120, Feb. 2007.

[12] T. Becker, M. Kluge, J. Schalk, K. Tiplady, C. Paget, U. Hilleringmann, and T. Otterpohl, "Autonomous sensor nodes for aircraft structural health monitoring," *IEEE Sensors J.*, vol. 9, no. 11, pp. 1589–1595, Nov. 2009.

[13] S. Arms, J. Galbreath, C. Townsend, D. Churchill, B. Corneau, R. Ketcham, and N. Phan, "Energy harvesting wireless sensors and networked timing synchronization for aircraft structural health monitoring," in *Proc. 2009 1st International Conference on Wireless Communication, Vehicular Technology, Information Theory and Aerospace & Electronic Systems Technology (VITAE'09)*. Aalborg, Denmark: IEEE, May 2009, pp. 16–20.

[14] M. R. Pearson, M. J. Eaton, R. Pullin, C. A. Featherston, and K. M. Holford, "Energy harvesting for aerospace structural health monitoring systems," *J. Phys.: Conf. Ser.*, vol. 382, Aug. 2012, 012025.

[15] R. W. Ziolkowski, "Low profile, broadside radiating, electrically small Huygens source antennas," *IEEE Access*, vol. 3, pp. 2644–2651, 2015.

[16] M.-C. Tang, T. Shi, and R. W. Ziolkowski, "A study of 28 GHz, planar, multilayered, electrically small, broadside radiating, Huygens source antennas," *IEEE Trans. Antennas Propag.*, vol. 65, no. 12, pp. 6345–6354, 2017.

[17] W. Lin, R. W. Ziolkowski, and J. Huang, "Electrically small, low-profile, highly efficient, Huygens dipole rectennas for wirelessly powering Internet-of-Things devices," *IEEE Trans. Antennas Propag.*, vol. 67, no. 6, pp. 3670–3679, Jun. 2019.

[18] R. W. Ziolkowski, "Custom-designed electrically small Huygens dipole antennas achieve efficient, directive emissions into air when mounted on a high permittivity block," *IEEE Access*, vol. 7, pp. 163 365–163 383, Jul. 2019.

[19] E. Borgia, "The Internet of Things vision: Key features, applications and open issues," *Comput. Commun.*, vol. 54, pp. 1–31, Dec. 2014.

[20] T. A. Klar, A. V. Kildishev, V. P. Drachev, and V. M. Shalaev, "Negative-index metamaterials: Going optical," *IEEE J. Sel. Topics Quan. Electron.*, vol. 12, no. 6, pp. 1106–1115, Jun. 2006.

[21] T. Suzuki and H. Asada, "Reflectionless zero refractive index metasurface in the terahertz waveband," *Opt. Express*, vol. 28, no. 15, pp. 21 509–21 521, Jul. 2020.

[22] W. Hong, K.-H. Baek, Y. Lee, Y. Kim, and S.-T. Ko, "Study and prototyping of practically large-scale mmwave antenna systems for 5G cellular devices," *IEEE Commun. Mag.*, vol. 52, no. 9, pp. 63–69, September 2014.

[23] Z. Pi and F. Khan, "An introduction to millimeter-wave mobile broadband systems," *IEEE Commun. Mag.*, vol. 49, no. 6, June 2011.

[24] T. S. Rappaport, S. Sun, R. Mayzus, H. Zhao, Y. Azar, K. Wang, G. N. Wong, J. K. Schulz, M. Samimi, and F. Gutierrez, "Millimeter wave mobile communications for 5G cellular: It will work!" *IEEE Access*, vol. 1, pp. 335–349, May 2013.

[25] W. Hong, K.-H. Baek, and S. Ko, "Millimeter-wave 5G antennas for smartphones: Overview and experimental demonstration," *IEEE Trans. Antennas Propag.*, vol. 65, no. 12, pp. 6250–6261, 2017.

[26] J. D. Jackson, *Classical Electrodynamics*. Hoboken, NJ: John Wiley & Sons, 1962.

[27] C. A. Balanis, *Advanced Engineering Electromagnetics*, 2nd ed. Hoboken, NJ: John Wiley & Sons, 2012.

[28] C. R. Paul, *Introduction to Electromagnetic Compatibility*. Hoboken, NJ: John Wiley & Sons, 2006, vol. 184.

[29] X. Qing, C. K. Goh, and Z. N. Chen, "Impedance characterization of RFID tag antennas and application in tag co-design," *IEEE Trans. Microw. Theory Techn.*, vol. 57, no. 5, pp. 1268–1274, May 2009.